Highlights

Numerical simulations of thixotropic semi-solid aluminium alloys in open-rotor and rotor-stator mixers

Imanol Garcia-Beristain[1], Michelle Figueroa-Landeta, J. Esteban López-Aguilar, Maider Garcia de Cortazar, Franck Girot, Marco Ellero

- BMP model provides appropriate behaviour to model thixo-viscoelastic Al-alloys
- Inter-blade zone vortices correlate with flow-structure and thixo-viscoelasticity
- 2D open-rotor and rotor-stator High Shearing Mixer heads where simulated
- Shear-thinning near rotor tips motivates relatively larger deformation-rates
- Thixo-viscoelasticity influences mixing rates between the rotor-stator and the bulk

[1]Corresponding author - Email: igarcia@bcamath.org

Numerical simulations of thixotropic semi-solid aluminium alloys in open-rotor and rotor-stator mixers

Imanol Garcia-Beristain[1a], Michelle Figueroa-Landeta[b], J. Esteban López-Aguilar[b], Maider Garcia de Cortazar[c], Franck Girot[d,e], Marco Ellero[a,e,f]

[a]*Basque Center for Applied Mathematics (BCAM), Alameda de Mazarredo 14, Bilbao, 48009, Bizkaia, Spain*
[b]*Facultad de Química, Departamento de Ingeniería Química, Universidad Nacional Autónoma de México (UNAM), Ciudad Universitaria, Coyoacán, Mexico City, 04510, CDMX, Mexico*
[c]*TECNALIA, Basque Research and Technology Alliance (BRTA), , Astondo Bidea E-700, Derio, 48160, Bizkaia, Spain*
[d]*Department of Mechanical Engineering, Engineering School of Bizkaia, University of the Basque Country (UPV/EHU), Alameda de Urquillo, Bilbao, 48013, Bizkaia, Spain*
[e]*IKERBASQUE, Basque Foundation for Science, Calle de María Díaz de Haro 3, Bilbao, 48013, Bizkaia, Spain*
[f]*Zienkiewicz Centre for Computational Engineering (ZCCE), Swansea University, Bay Campus, Swansea, SA1 8EN, , United Kingdom*

Abstract

This research uses the Bautista-Manero-Puig (BMP) model to examine flow patterns of semi-solid aluminium alloys (Al) in open-rotor and stator-rotor mixers via numerical solutions. The model captures the distinct thixo-viscoelastic behavior of the Al-alloys at low temperatures, near melting point. The analysis involves using 2D structured-meshes for open-rotor and rotor-stator geometries. Solutions for Newtonian and thixo-viscoelastic model fluids are reported through fields of velocity, strain-rate, stress, fluidity, and streamlines, revealing distinct features. Findings reveal nonlinear thixo-viscoelastic vortex patterns that vary with rotational speed, resulting in different fluidity and stress profiles compared to the invariant response of Newtonian fluids. At lower rotational speeds, rotor-pallets are dominated by structured material that gradually becomes unstructured to cover the outer

[1]Corresponding author - Email: igarcia@bcamath.org

vessel walls. When including a stator, the inner stator region resembles the Newtonian solution, but the outflow through stator gaps is reduced due to flow-structure levels outside. This information is of interest for industrial design and optimization of molten Al-alloy processing.

Keywords: Semi-solid Al-alloys, Numerical simulation, BMP model, OpenFOAM/Rheotool

1. Introduction

In the context of circular economy, effective recycling of metal-based materials is of crucial importance. Casting and forming processes are used in most manufactured products and in almost all manufacturing machinery. Despite this, to date, primary metals obtained from the direct transformation of natural resources are almost exclusively used, incorporating very small amounts of secondary or recycled metals. Optimal recycling of aluminium would save 95% of the energy used in primary production and an equivalent reduction in CO2 emissions [2].

In the particular case of aluminium (Al) alloys, the problems when using recycled materials, and thus reducing the use of primary aluminium, are mainly related to impurities and defects. Iron (Fe) is the most common impurity in aluminium and its alloys. In particular, it cannot be easily removed and can cause adverse effects on ductility and processability of the resulting component. This is a critical mechanical problem, for example, in alloys used in casting processes such as Al-Si-based alloys. For these Al-Si-based alloys, molten primary aluminium typically contains between 0.02 - 0.15% by weight of iron. There is no known effective way to remove iron from aluminium, in such a way that these primary Fe values are the typical baseline and all the additional melting activities will potentially increase its level further.

To date, the alternatives to control the negative effect of iron on the microstructure of aluminium alloys are: (1) by addition of suitable neutralizers to chemically suppress specific shapes that embrittle alloys, while promoting instead growth of platelet-like of globular-shape Fe-morphologies [1, 2, 3, 4, 5]. (2) Try to mechanically modify the geometry of the Fe-intermetallic phases, or, in other words, breaking the acicular geometry of the Fe-phases to reduce them in size and give them a more spheroidal shape [6].

[2] https://www.european-aluminium.eu

In the latter case, it is crucial to develop novel technologies and processes that favour intermetallic phase fragmentation. Agitation and vibration are methods widely used during solidification for refining grains of aluminum. Various agitation methods have been employed for this purpose, including agitation mechanics, electromagnetic agitation and bubble mixing [7, 8]. It has been observed that material flow has a considerable effect on the microstructure and it is possible to transform needles-like Fe phases into blocks. During agitation, these acicular phases break based on a fracture mechanism [9, 10] caused by shear and viscous forces.

Existing methods for treating liquid metals by stirring include mechanical agitation by an impeller or propeller, electromagnetic agitation and some other, such as gas-induced liquid flow. Mechanical stirring using an impeller is a simple way to treat liquid metals. McRae et al. [11] describe a method of mechanical stirring of liquid metals to produce alloys. The process introduces a stirring device primarily to accelerate the dissolution of alloying elements and slow down slag formation.

Fan et al. [12] proposed a shaped rotor-stator device similar to an open impeller, but this rotor is closely surrounded by the stator with holes. This design allows the use of high speed, that is, the rotors rotate at an order-of-magnitude larger frequency than the open impellers in a stirred tank. Typically, blade tip (rotor) speed ranges from 10 to 50 m/s [13]. The rotor-stator gap ranges from 100 to 3000 μm and, since the local volume inside the gap is extremely small, the local energy dissipation rate can be three orders-of-magnitude higher than in a conventional shake. For this reason, such devices are generally known as High Shearing Mixers (HSM) [or, generally, High Shearing Processing (HSP)], since the highest shear-rates inside the sample can reach values from 20,000 to 100,000 s^{-1} [13]. The high shear-rate achieved inside these mixers effectively breaks up large oxide films of aluminium and clusters into fine individual particles.

It is therefore relevant to develop efficient and accurate Computational Fluid Dynamics (CFD) models able to predict the flow of liquid (at high temperature) or semi-solid (at moderate-low temperatures) Al-alloys in complex mixing geometries to optimize operating conditions and design.

Numerical analysis on this type of operations has been done recently in the context of liquid metals in Tong et al. [14], where CFD has been applied to perform HSP simulations in molten aluminium treated as a Newtonian liquid with constant dynamic viscosity ($\approx$ 0.0027 Pa·s). Such a full HSP-setup was solved with a SIMPLE scheme and simulated using the FLUENT

module of ANSYS. Moreover, under typical operating conditions in HSP, the blades rotate at angular velocities exceeding 1000 rpm, leading to effective Reynolds numbers larger than 40,000. Consequently, turbulence models are required to simulate the mixing flow of Al-alloys in the liquid state (i.e. at very high temperatures).

Despite the apparent simplicity related to the choice of a Newtonian description, such an assumption cannot generally hold for aluminium alloys. In fact, below a critical temperature ($\approx 590°$C for A380 [15]), alloys undergo liquid-solid transition and start showing significant temperature effects (i.e. on viscosity $\eta(T)$), as well as highly non-Newtonian properties. In particular, due to the presence of a coarsening/re-arranging solid phase, the following responses are observed: a) shear-thinning, i.e. a decrease of the Al-alloy viscosity with increasing shear-rates and shear-thickening at high shear-rates [16, 17, 18]; b) thixotropy, observed as a transient response of the viscosity to an applied stress [19]; and c) viscoelastoplasticity [20]. A recent review on the rheological characterization of semi-solid metals is given in [21].

Early numerical approaches incorporate non-Newtonian effects by properly tuning the shear-rate dependence of a variable viscosity function against rheometrical data. Examples include simple homogeneous power-law viscous models with temperature-dependent viscosity, which were implemented into a commercial finite-element software to simulate mould-filling operations during the semi-solid processing (thixoforming) of aluminium alloys [22]. Other shear-thinning/thickening power-law and Carreau-Yasuda models were used in [23]. However, in present times, it is widely acknowledged that these time-independent models tuned on steady-state rheological data cannot capture the complex transient response of aluminium alloys.

It is well known that heterogeneous microstructure formation (e.g. local solidification, particle coarsening, aggregation, among others) occurs over a finite timescale during material processing [24]. To establish control over it, a scalar field describing the heterogeneous microstructure evolution accounts for the density or state of the dispersed crystalline or solid phase [25, 26, 27, 28]. However, these studies focus on the microstructure kinetics in semi-solid aluminium alloys, whereas no explicit link is established between the time-dependent microstructure and the resulting macroscopic rheology of the fluid. In [29], a proposal of such a micro-macro link is given, but, to the best of our knowledge, the model has not been applied to realistic flowing conditions, whereas in [30], time-dependent effects were incorporated in a power-law shear-thinning model for A319 alloys using viscosity data obtained under

compressive tests.

A more formal way to incorporate time-dependent viscous effects (i.e. thixotropy) due to a changing microstructure, is through micro-mechanical-continuum models, where the constitutive parameters are coupled to the concurrent evolution of an additional microstructural variable (sometimes denoted as structure or coherency parameter) [21]. In [31], a minimal microstructural model was proposed and linked to a viscosity function. In [32], parameters in a viscoplastic Herschel-Bulkley fluid model were linked to a kinetic equation for a structure parameter. A similar time-dependent Herschel-Bulkley model was used in [33] and implemented into a CFD software (FLOW 3D) to simulate steel semi-solid metal forming and die injection process.

Many of these models have been used in the context of cold metal extrusion processes using finite elements or meshless discretization of visco-elasto-plastic equations. For example, Chen et al. [34] have used a rigid-plastic finite-element DEFORM 3D software to investigate the plastic deformation behavior of an aluminium billet during its axisymmetric extrusion through a conical die. Bastani [35] also used a finite-element code to optimize the shape and mechanical properties in an aluminium extrusion process. In [36], the application of the Natural Element Method (NEM) for simulating forming processes involving large displacements was described. Later, the method was applied to 3D simulations of aluminium extrusion where the material was modelled as a rigid-plastic material governed by a SellarsTegart-type law [36]. In the context of the Smoothed Particle Hydrodynamics method (SPH), applications to liquid metal (initially modelled as Newtonian liquids) in high-pressure die-casting processes were discussed in [37, 38]. This method was later modified to incorporate elasto-plastic deformation [39] following the Jaumann or Maxwell SPH viscoelastic models proposed initially in [40, 41]. More recently, full elasto-viscoplastic SPH models have been used in complex metal forging processes [42].

These methods have not been applied yet to the specific rotor-based mixers targeted in this paper. Moreover, for semi-solid aluminium alloys at low/moderate solid volume fractions, elastic effects are considered negligible and viscoplastic models are still adequate, but thixotropy is essential [43]. To the best of our knowledge, no thixotropic model has been applied so far to the CFD analysis of semi-solid alloys in a realistic HSP setup, where only Newtonian computations have been made to date [14].

An approach naturally incorporating thixotropic and viscoelastoplastic

features into material response has been recently used in the context of wormlike micellar solutions in [44, 45, 46] under the Bautista-Manero-Puig (BMP) family of fluids. These BMP constitutive equations incorporate time-dependent thixotropic features through a structure equation written for fluidity. Here, a construction-destruction dynamics is modulated by a structure-construction timescale and an inverse characteristic stress for structure destruction, which drives non-linearity using the energy dissipated by the viscoelastic fluid in motion. This fluidity connects with stress via the non-Newtonian viscosity in an Oldroyd-B-like differential constitutive equation. These models have been tested in complex flow scenarios, ranging from rounded and sharp contraction-expansion geometries [45] and flow past a sphere [46].

In this article, we introduce thixotropy and viscoelasticity in the analysis using the BMP model and show that non-Newtonian properties of semi-solid aluminium alloys have a significant impact on the computed stress field and, in conclusion, on the operating conditions for HSP for these systems. Here, we use OpenFOAM [47], which is a versatile open-source finite-volume library supporting arbitrary polyhedral meshes. The source code has been designed to create solvers from a high-level abstraction code manipulation. Hence, it is a popular framework to create high-performance solvers for many applications. A recent extension to the field of non-Newtonian fluid mechanics is provided by rheoTool [48], which is often used in rheological applications. RheoTool includes state-of-the-art numerical schemes and fluid models to improve stability and accuracy to describing highly non-Newtonian complex flows. Here a version of the BMP model will be considered to effectively modelling matrix thixotropic effects based on a coupled formation/destruction microstructural dynamics.

The structure of the paper is the following one: In Section 2 the governing equations are described in terms of the mass-momentum balance doublet alongside the thixo-viscoelastic BMP constitutive equation. In Section 3 the essential features of the finite-volume-based OpenFOAM algorithm are described. In Section 4 its discretization is provided alongside the material functions relevant to the Al-alloy and its characterisation using the BMP model. In Section 5, numerical Results are provided in terms of deformation-rate, fluidity, stress and streamline fields, in which evidence of the influence of viscoelasticity and thixotropy is exposed. Finally, in Section 6 the final remarks and achievements of this work are provided.

2. Thixotropic Model: Governing Equations

The governing equations are based on mass and momentum conservation in a rotational reference frame, as follows (eq 7.9 in [49]):

$$\nabla \cdot \boldsymbol{w} = 0, \tag{1}$$

$$\rho \left(\frac{\partial \boldsymbol{u}}{\partial t} + \boldsymbol{w} \cdot \nabla \boldsymbol{u} + \boldsymbol{\Omega} \times \boldsymbol{u} \right) = -\nabla p + \nabla \cdot \boldsymbol{\tau}, \tag{2}$$

where t represents time, $\boldsymbol{u} = \boldsymbol{w} \times \boldsymbol{r}$ and $\boldsymbol{w}$ are absolute and relative velocities in the rotating frame, $\boldsymbol{\Omega}$ is the rotational angular velocity, which for current 2D case is $\boldsymbol{\Omega} = (0, 0, \omega)$. Finally, p and $\boldsymbol{\tau}$ are pressure and total extra-stress field variables, respectively. The extra-stress $\boldsymbol{\tau}$ is decomposed into two additive parts: the Newtonian (viscous-inelastic) solvent component $\boldsymbol{\tau}_s$ and the extra non-Newtonian stress contribution $\boldsymbol{\tau}_p$:

$$\boldsymbol{\tau} = \boldsymbol{\tau}_s + \boldsymbol{\tau}_p. \tag{3}$$

Both stress components require further modelling, relating them to field variables. The solvent stress contribution is modelled as an equivalent Newtonian formulation:

$$\boldsymbol{\tau}_s = \eta_s \left(\nabla \boldsymbol{u} + \nabla \boldsymbol{u}^{\mathrm{T}} \right) = 2\eta_s \boldsymbol{D}, \tag{4}$$

where the deformation-rate tensor has the property of being equivalent in inertial and rotational reference frames,

$$\boldsymbol{D} = \frac{\nabla \boldsymbol{u} + \nabla \boldsymbol{u}^T}{2} = \frac{\nabla \boldsymbol{w} + \nabla \boldsymbol{w}^T}{2}. \tag{5}$$

The extra stress $\boldsymbol{\tau}_p$ is modelled using the Bautista-Manero-Puig (BMP) constitutive model [44, 45, 46, 50] in a rotational reference frame, which is based on a differential viscoelastic model of the Oldroyd-B-type:

$$\varphi G_0 \boldsymbol{\tau}_p + \overset{\nabla}{\boldsymbol{\tau}}_p = 2G_0 \boldsymbol{D}, \tag{6}$$

with the fluidity being function of the deformation-rate tensor, $\varphi(\boldsymbol{D})$, and G_0 is the instantaneous elastic modulus measured at vanishing deformation-rates. The rotating frame upper-convected time derivative of the extra non-Newtonian stress is defined as:

$$\overset{\nabla}{\boldsymbol{\tau}}_p = \frac{\partial \boldsymbol{\tau}_p}{\partial t} + \boldsymbol{w} \cdot \nabla \boldsymbol{\tau}_p - \boldsymbol{\tau}_p \cdot \nabla \boldsymbol{w} - \nabla \boldsymbol{w}^{\mathrm{T}} \cdot \boldsymbol{\tau}_p. \tag{7}$$

The fluidity space-time evolution describes thixo-viscoelastoplastic behaviour by modelling the construction-destruction dynamics of the fluid's internal network structure [44, 45, 46]. The present paper uses the following implementation [50]: the fluidity equation is solved in a relative velocity framework, and after, a conversion of the absolute velocity variable ($\boldsymbol{u}$ in Eq. 2) into a rotating-frame velocity ($\boldsymbol{w}$) is performed:

$$\frac{\partial \varphi}{\partial t} + \boldsymbol{w} \cdot \nabla \varphi = \frac{\varphi_0 - \varphi}{\lambda_s} + k \left(\varphi_\infty - \varphi \right) \boldsymbol{\tau}_p : \boldsymbol{D}, \tag{8}$$

where φ_0 is the fluidity level at vanishing deformation-rates, and φ_∞ is the fluidity in the high deformation-rate limit. Note that the following equivalences holds: $\eta_p \equiv 1/\varphi$, $\eta_{p0} \equiv 1/\varphi_0$ and $\eta_{p\infty} \equiv 1/\varphi_\infty$. The terms on the RHS of Eq. (8) represent the microstructure construction and destruction rates, respectively. Structure construction is calibrated through a thixotropic timescale λ_s, whereas structure destruction is proportional to both the kinetic constant for structure breakdown, k, which has units of inverse of stress, and the dissipation function originating from the non-Newtonian stress tensor, $\boldsymbol{\tau}_p : \boldsymbol{D}$. In the limit of $\lambda_s \to 0$, the time for internal-structure construction reduces to null times; in this case, the fluid recovers its internal structure very quickly, displaying a large viscosity and needing stronger flows to break its structure and display non-linear features, e.g. shear-thinning, extension hardening and softening and normal stresses.

If dimensionless variables are introduced viz.:

$$\begin{aligned} p' &= \frac{p}{(\eta_{p0} + \eta_s)\,\omega}, & \varphi' &= \varphi\,\eta_{p0}, \\ \boldsymbol{\tau}' &= \frac{\boldsymbol{\tau}}{(\eta_{p0} + \eta_s)\,\omega}, & \mathbf{u}' &= \frac{\mathbf{u}}{\omega\,L}, \\ \mathbf{r}' &= \frac{\mathbf{r}}{L}, & \nabla' &= L\nabla, \\ t' &= \omega t, \end{aligned} \tag{9}$$

the following dimensionless numbers can be defined: the Reynolds number $Re = \rho\omega L^2/(\eta_s + \eta_{p0})$, which represents the ratio of inertial to viscous forces at vanishing deformation-rates; the Weissenberg number $Wi = \lambda_1\omega$, defined as the product of the characteristic material relaxation-time ($\lambda_1 = \eta_{p0}/G_0$) and the characteristic deformation-rate given by the angular rotational speed ω; a solvent-fraction number $\beta = \eta_s/(\eta_{p0} + \eta_s)$, which is related to the proportion of the total stress given by the Newtonian solvent relative to that of the

non-Newtonian solute at vanishing deformation-rates. Finally, thixotropy is modulated by a structure construction dimensionless time $\Omega = \lambda_s \omega$ and a dimensionless structure-destruction stress $\xi = k(\eta_{p0} + \eta_s)\omega$.

Additionally, the following scalar second invariant of the non-Newtonian stress can be defined and used as a representative measure of its magnitude:

$$\tau_{eq} = \sqrt{2\boldsymbol{\tau}'_p : \boldsymbol{\tau}'_p}, \tag{10}$$

where $\boldsymbol{\tau}'_p$ is the dimensionless non-Newtonian stress.

3. Numerical Algorithm: OpenFOAM & the Finite Volume Method

Numerical solution to the momentum-mass conservation equations and rheological equation-of-state is performed with the open-source software OpenFOAM in conjunction with rheoTool [50, 48, 51]. Numerical discretization for convective divergence terms were done using a second-order upwind-based scheme with velocity-gradient limiters. Time discretization is done with an implicit Euler scheme. A segregated SIMPLEC with stress-velocity coupling stabilization in the momentum predictor is used. Stabilization is obtained by adding a fourth-order velocity derivative to the non-Newtonian extra-stress divergence discretization:

$$\int_V (\nabla \cdot \boldsymbol{\tau}_p) \mathrm{d}V = \int_V \nabla \cdot \overline{\boldsymbol{\tau}}_p \mathrm{d}V + \int_V \nabla \cdot (\eta_p \nabla \mathbf{u}) \, \mathrm{d}V - \int_V \overline{\nabla \cdot (\eta_p \nabla \mathbf{u})} \mathrm{d}V. \tag{11}$$

The overbar on the first and third terms on the RHS of Eq.(11) indicates a linear interpolation to the cell faces, whereas the second term is the Laplacian operator, which is evaluated directly from cell-centered velocities straddling the face. The difference in the evaluation of the two Laplacian-operator types generates a coupling effect between stress and velocity when solving the momentum equation. Using a both-side-diffusion technique, by which the cell-centered contribution is evaluated implicitly and the rest of the non-Newtonian contribution is computed explicitly, the momentum balance in Eq. 2 is rewritten as:

$$\rho \left(\frac{\partial \boldsymbol{u}}{\partial t} + \boldsymbol{w} \cdot \nabla \boldsymbol{u} + \boldsymbol{\Omega} \times \boldsymbol{u} \right) - \nabla \cdot (\eta_s + \eta_p) \nabla \boldsymbol{u} = \quad -\nabla p + \nabla \cdot \overline{\boldsymbol{\tau}}_p - \overline{\nabla \cdot \eta_p \nabla \boldsymbol{u}}, \tag{12}$$

where all the RHS terms are the explicit components. Such stabilization procedure is of importance for low values of solvent-fraction β, and in particular for Upper-Convective Maxwell models ($\beta = 0$) [48].

In addition to velocity-stress coupling, a *log-conformation* stabilization has been used. Log-conformation is a popular strategy used to avoid the exponential growth of stress conformation tensor at high Weissenberg numbers. It uses a reformulation of the constitutive equation in a log-based stress variable, which keeps the conformation tensor positive definite and linearises the stress field in regions of exponential growth, leading to enhanced numerical stability [48]. The conformation tensor $\boldsymbol{A}$ is related to the stress-tensor as follows:

$$\boldsymbol{\tau} = \frac{\eta_p}{\lambda_1}(\mathbf{A} - \mathbf{I}). \tag{13}$$

Due to its positive definiteness, $\boldsymbol{A}$ can be decomposed $\boldsymbol{A} = \boldsymbol{R}\boldsymbol{\Lambda}\boldsymbol{R}^T$. The log-conformation tensor is then defined as:

$$\boldsymbol{\Theta} = \ln(\boldsymbol{A}) = \mathbf{R}\ln(\boldsymbol{\Lambda})\mathbf{R}^{\mathrm{T}}, \tag{14}$$

which is used to solve a modified viscoelastic formulation by re-casting Eq. 6.

To ensure the capture of the relevant non-linear phenomena in the form viscoelasticity and thixotropy, solutions were computed using a Courant number of $C = \frac{U\Delta t}{\Delta h} = 0.4$ for all meshes, with time-step sizes ranging from 3×10^{-3} for M1 at 1 rad/s to 10^{-5} for M4 at 10 rad/s. Here, U is a characteristic velocity given by relevant angular velocity and the rotor radius, Δt is the time-step size and Δh is a characteristic length of the mesh. Regarding the linearized matrix solvers, the preconditioned bi-conjugate gradient family of solvers has been used to solve the field variables, with an absolute convergence criterion of 10^{-13} error tolerance for each iteration. Results are converged to residual values of 10^{-7}.

4. Problem Description

In this section, the Newtonian and thixotropic parameters of the fluid and the computational set-up are presented.

4.1. Thixo-viscoelastic BMP rheology

The current mixer application with highly viscous molten alloys is run under creeping-flow conditions with maximal Reynolds numbers in the order of

10^{-2} (see section 4.2), which permits to analyse the predictions with only one source of non-linearity, i.e. thixo-viscoelasticity. The numerical solutions presented in this paper are performed using the BMP model mentioned above. This constitutive model captures the main features of semi-solid aluminium alloys, i.e. strong shear-thinning accompanied by thixotropy and non-linear viscoelasticity [15]. As an illustrative example, in Fig. 1, the steady-state and transient shear viscosity data for an A380 aluminium alloy at T={530,550} °C are plotted from [15]. This information helps to identify the common and defining features of molten Al-alloys, i.e. a steep drop of its steady shear-viscosity with shear-rate, that may amount to several orders-of-magnitude (see Fig. 1-top), and a time-dependent response in the form of thixotropy (see Fig. 1-bottom). The corresponding BMP fitting predictions are provided in continuous lines under the parameter-settings in Table 1. For this fitting, a deformation-rate-dependent structure-destruction coefficient k is considered, particularly specified in a linear relationship, i.e. $k = k_0(1 + \zeta\dot{\gamma})$; here, ζ is the so-called shear-banding intensity parameter [52, 53]. Such linear deformation-rate functionality of the structure-destruction coefficient has already been used in the context of shear-banded flows of wormlike micellar solutions [52, 53]. As illustrated in Fig.1, the BMP model can reproduce faithfully the rheological response typically reported for Al-alloys [15]. Particularly to the transient tests, revealing thixotropic features in Fig.1b, structure-destruction parameter-adjustment is required for step-up and step-down phases. These results reflect the highly complex rheological response of Al-alloys and justify the use of complex rheological equations-of-state in their characterisation, such as the BMP model. Being this work a first attempt to model Al-alloy rheology with the BMP model, a simpler parameter specification is used for computations (related to solution-attainability) and the solutions illustrated in the Results section, i.e. taking $\zeta = 0$; see on to Section 5 for further details.

Table 1: BMP model parameters fitting experimental data reported by Solek and Szczepanik [15].

Temperature (C)	530	550
η_{p0} (Pa s)	1×10^4	1×10^3
η_∞ (Pa s)	8×10^{-2}	8×10^{-2}
η_s (Pa s)	1×10^{-2}	1×10^{-2}
λ_1 (s)	1	1
λ_s (s)	50	50
Step-up phase		
k_0 (Pa^{-1})	1.66×10^{-10}	1.60×10^{-8}
ζ (s)	0.93	0.19
Step-down phase		
k_0 (Pa^{-1})	3.08×10^{-9}	4.73×10^{-8}
ζ (s)	0.04	0.06

4.2. Mixer-head geometry

In this work we consider a mixer head under two configurations. A first case for an open rotor without a stator and a second case a coupled rotor-stator device.

A two-dimensional round-edged rotor is used to generate shearing motion on the molten aluminium (see Figure 2). Initially, no stator is considered as a first step to understand the limitations of an open rotor mixer for semi-solid aluminium applications. The rotor has a 55 mm diameter with 4 blades of 7 mm blade-thickness. The blade edges have been rounded with a 1 mm inner radius, whereas the joints between the blades have a 5 mm rounding radius. Therefore, all curves are tangent to the adjacent straight section in the blades.

Geometry discretization and mesh-convergence verification has been performed on four levels of mesh refinement. discretization properties of each mesh are given in Table 2. Figure 2 shows mesh M3 alongside zoomed representations of the rotor-blade tip and the rotor hub for all meshes M1-M4.

Particular attention has been paid to velocity-gradient calculation given its mesh-quality sensitivity. Here, structured meshes result in improved-quality solutions compared to those obtained with unstructured meshes. The current geometry has been discretized using linear quadrilaterals by a boundary extrusion method. A layer growth-rate of 1.05 has been used until an

Table 2: Mesh parameters

	M1	M2	M3	M4
Number of elements	210,180	338,364	1,044,320	4,676,756
Number of nodal points	421,600	678,656	2,092,544	9,366,000
Number of elements in rotor tip	9	18	80	160
Boundary layer element size	5e-5	2.5e-5	1E-5	5E-6

apparently uniform aspect-ratio is obtained, point from which the growth-rate is set to zero.

After validation of the open-rotor geometry, the mixing head with an additional stator is simulated and analyzed. The stator includes 15 squares with a 3 mm side length. The gap between the stator and the rotor is 1.15 mm. Simulations are run with mesh M2 for which the stator-free case at the rotor surface has previously shown numerical convergence.

4.3. Boundary and Initial Conditions

Wall conditions are imposed on all boundary surfaces for the rotating reference frame. The impeller has an absolute velocity value $\boldsymbol{u} = \boldsymbol{\Omega} \times \boldsymbol{r}$, and the stator and the outer boundary conditions are $\boldsymbol{u} = 0$. Pressure, fluidity and stress variables do not require boundary value prescription, but being a collocated-type solver values need to be computed from the cell center into the boundary face center [54, 50]. Zero-gradient extrapolation is used for pressure and fluidity, whereas linear extrapolation is used for stress by first computing the gradient by the Gauss method and then computing the extrapolation according to the formula: $\tau_{p_{\mathrm{ij},f}} = \tau_{p_{\mathrm{ij,P}}} + \left(\nabla \tau_{p_{\mathrm{ij}}}\right)_{\mathrm{P}} \cdot \mathbf{d}_{\mathrm{Pf}}$, $\tau_{p_{\mathrm{ij}}}$ is the ij component of the viscoelastic stress; f and P represent the boundary face and the cell center value owning that face, respectively; $\mathbf{d}_{\mathrm{Pf}}$ is the vector connecting their geometrical centers.

As initial conditions, pressure and velocity fields were set up as zero for the Newtonian case, and uniform zero and one non-Newtonian stress and fluidity respectively. The viscoelastic case was initialized from a corresponding Newtonian solution according to the continuation procedure described in Section 5.

5. Numerical results of the open-rotor mixer

For Al alloys, taking as a reference the experimental data in [15] and the BMP model fitting in Fig. 1, with a typical rotational-speed of 60 rad/s ($\approx$ 600rpm), the following dimensionless parameters arise: $\{\beta, Re, Wi, \Omega, \xi\} = \{10^{-5}, 4.4 \times 10^{-4}, 60, 3000, 6 \times 10^{-5}\}$. In order to have a simple numerically-tractable case and given that this problem has not been tackled using a complex constitutive equation that reflects the thixo-viscoelastic properties of Al-alloys [15], such as the BMP model, we have chosen a set of parameters that captures the essential aluminium-alloy rheological response under conditions that warrant solution stability, i.e. $\{\eta_{p0}, \eta_s, \eta_{p\infty}, G_0, \lambda, k\} = \{99, 1, 10^{-4}, 99, 0.4, 10^{-5}\}$. With this parameter-set the following dimensionless values hold: $Re = \rho\omega L^2/(\eta_s + \eta_{p0}) \approx \omega \times 7.3 \times 10^{-6}$, where ω is the rotational speed and L the rotor radius (27.5 mm); the solvent-fraction is $\beta = 0.01$; viscoelasticity is modulated by the rotational frequency, i.e. $Wi = \eta_{p0}\omega/G_0 = \lambda_1\omega$, as it happens with the thixotropic parameters. [15] Fig. 1

As given by the definition of the Weissenberg number in the previous section, there is a direct proportionality between this dimensionless number and the rotational speed of the rotor. Such relationship becomes a limiting factor to getting high rotational speed viscoelastic simulations. This embodies the well-known 'High Weissenberg Number Problem' ceiling for the present flow problem. With the present numerical framework, the last stable solution before locating the critical Weissenberg number Wi_{crit} found for the M4-geometry and the chosen parameter-set, i.e. $\{\eta_{p0}, \eta_s, \eta_{p\infty}, G_0, \lambda, k\} = \{99, 1, 10^{-4}, 99, 0.4, 10^{-5}\}$, is $Wi_{stable} = 14$.

The strategy followed to generate viscoelastic solutions consists of two steps: (i) a Newtonian solution was obtained at rotational velocity $\omega = 1$ rad/s with viscosity $\eta_s = 100$ (corresponding to the first Newtonian-plateau level chosen in the BMP model) and density $\rho = 1$. (ii) A thixo-viscoelastic solution at $\omega = 1$ rad/s is computed from the Newtonian result in (i) to improve stability. (iii) Thixo-viscoelastic solutions for higher rotational speeds are obtained by continuation: increasing the rotational velocity by 1 rad/s stepwise until the last stable solution is obtained and beyond which the simulation diverges.

In this section, a comparative description is provided for a relatively low and a near critical Weissenberg values, i.e. $Wi = \{1, 10\}$. Figures 4-9 illustrate solutions for the whole geometry in terms of the dimensionless velocity,

fluidity, stress and strain-rate. A common scale has been fixed across Wi-levels to allow qualitative comparison.

5.1. Flow-field Description

5.1.1. Bulk zone

In Fig. 4(a)-(c), contrasting velocity distributions between Newtonian and viscoelastic solutions are apparent. Here, the Newtonian solutions display a more mobile material than that observed for the viscoelastic solution at both rotational speeds analysed; indeed, no difference is detected across rotational-speed levels under the Newtonian settings, with shear-rates different to zero occupying half of the flow domain. In contrast, the thixo-viscoelastic case starts with motion confined to the rotor surrounding area at Wi=1, whilst rotational speed increase to Wi=10 makes the velocity field increase in magnitude towards the outer walls of the container. This is reflected in the deformation-rate fields in Fig. 4 (h)-(j), for which strain-rate at Wi=10 appears an order-of-magnitude larger than that for Wi=1 in a considerable area of the outer region close to the outer non-rotating boundary. Nevertheless, both cases have similar maxima on the rotor tips with a higher mean in the surrounding area for Wi=1.

The consequences of such deformation-rate fields on flow structure are observed in Fig. 4(d) and (e) through fluidity field contours. At Wi=1, the flow domain is filled with a highly-structured material in the outer region and in the gaps between the rotor blades, zones under which relatively lower strain-rate values are present. Fluidised material is located only near the rotor-tip surroundings. In contrast, for the Wi=10 solution, the field is dominated by a highly-unstructured material. At this Wi-level fluidity ranges from $10 \leq \varphi' = \eta_{p0}/\eta_p \leq 10^3$, which reflects a change in viscosity between one and three orders-of-magnitude from η_{p0}.

Stress follows these fluidity trends holding their inverse relationship, as illustrated in Fig. 4 (f) and (g). Here, the Wi=1 solution displays a four-petal flower-like red fringe with relatively larger stress values; this structure vanishes at Wi=10 with a stress-level decrease of some one-to-two orders-of-magnitude and a nearly plane field amounting levels of $O(10^{-2})$.

5.1.2. Inter-blade kinematics

The space between blades near the rotor displays notable features in the form of recirculation response to the fluid rheology. The flow-field description in these inter-blade regions can be split into two main areas separated by the

recirculation zone. Fig. 5 shows, with the help of streamline contours, a recirculation zone spanning between points III and V, which covers half of the inter-blade gap. Here, an anti-clockwise vortex is generated within each pair of blades. The shape of the vortex convexity is influenced by the change in rheology. This is apparent in the comparison between the Newtonian to the thixo-viscoelastic solutions.

Comparing the Newtonian fluid with the Wi=1 in Fig.5 (a) and (c) respectively the Newtonian fluid responds with a weaker vortex whose boundary appears flatter than that of the stronger markedly-convex thixo-viscoelastic vortex. Comparison between thixo-viscoelastic $Wi = 1$ and $Wi = 10$ strain-rates in Fig. 5 (c) and (d), respectively, reveals a weakening of the vortex with rotational-speed increase, making the higher Wi case concave, which may be caused by the strong shear-thinning properties of thixo-viscoelastic Al-alloys (see Fig. 1).

These trends in inter-blade flow-structure and kinematics are intimately related to and their connection with fluidity (Fig. 6 (a) and (b)). For $Wi = 1$ in Fig. 6(a), the vortex region in between the blades appears filled with a red shading corresponding to a fluidity level near to unity; this translates into large viscosities in the first Newtonian plateau and a fully-structured alloy. Increase of rotational speed to Wi=10 in Fig. 6(b) leads to fluidity values in the range from unity to around 100 units in the inter-blade gap, which maps the viscosity and first normal-stress difference into the shear-thinning response (recall the shear-thinning steady-state material properties of the BMP model, i.e. viscosity $\eta_{Shear} = \eta_s + \frac{1}{\varphi}$ and first normal-stress difference $N_{1Shear} = \frac{2\lambda_1\dot{\gamma}^2}{\eta_{p0}\varphi^2}$ [55], for which an inverse relationship between fluidity and shear viscosity-N_{1shear} holds). Correspondingly, stress levels decline with Wi-rise as it is apparent in Fig. 6(c) and (d).

5.2. Convergence analysis

In this section, results on mesh-convergence are assessed by comparing rotor torque forces and field values along S1 and S2 trajectories (represented in Fig. 2) for refinement levels from M1 to M4. Additionally, the influence of viscoelasticity is discussed in such results.

5.2.1. Integral value convergence: Torque

Dimensionless viscous (T'_η) and pressure (T'_p) induced torque is investigated for Newtonian and viscoelastic fluids. These quantities are defined as

follows:

$$T'_\eta = \int_{\text{blade}} \boldsymbol{r}' \times (\mathbf{WSS} - \hat{\boldsymbol{n}} \cdot (\mathbf{WSS} \cdot \hat{\boldsymbol{n}})), \tag{15}$$

$$T'_p = \int_{\text{blade}} \boldsymbol{r}' \times (p' \hat{\boldsymbol{n}}), \tag{16}$$

where $\hat{\boldsymbol{n}}$ is the wall normal vector and **WSS** is the wall shear stress defined as,

$$\mathbf{WSS} = \hat{\boldsymbol{n}} \cdot \boldsymbol{\tau}'. \tag{17}$$

Recall p' is the dimensionless pressure defined in Eq. 9. $\boldsymbol{r}'$ is the dimensionless relative position to the rotation axis vector also found in Eq. 9. Finally, $\boldsymbol{\tau}'$ is the contribution of both dimensionless Newtonian and non-Newtonian extra-stress according to Eq. 9 and 3.

Solutions are summarized in Tables 3 and 4, in which, for reference, absolute dimensionless values are given between brackets for the Newtonian M1 case. Torque values are normalized with respect to the corresponding Newtonian M1 case at each rotational speed.

Viscosity and pressure-induced (dimensionless) torque remain constant for the Newtonian case at both rotational speeds; i.e. $T'_\eta = 0.00345$ units for the viscous contribution and $T'_p = 0.00495$ units for the pressure contribution, evidencing a linear scaling between the torque-measures and the rotational speed, as expected in a Stokesian regime.

Thixo-viscoelastic results show a strong non-linear torque behaviour with the rotational speed, measured here through Wi-change. At Wi=1, the viscoelastic viscous torque T'_η is 0.0366, and drops some three times to levels around 0.015 with the frequency increase to Wi=10. This correlates with the extreme shear-thinning properties of the material (see Fig. 1). The viscoelastic pressure torque T'_p-reduction has a similar behaviour. Here, T'_p-values at $Wi = 1$ is 0.0064, whilst at Wi=10, this torque contribution amounts only 0.017 units.

Torque values converge up to the third decimal position when comparing different refinement levels from M1 to M4, as listed in Tables 3 and 4. Hence, a mesh density equivalent to M2 (496,692 elements) is used throughout the stator case, leading to a balance between accuracy and computational effort in the solution acquisition.

Table 3: Viscosity induced dimensionless torque normalized with respect to the Newtonian value for the corresponding rotational velocity. Absolute dimensionless value is given between braces.

ω	T'_η	M1	M2	M3	M4
1	Thixotropic	0.0368	0.0368	0.0368	0.0366
	Newtonian	1.0 (-0.00345)	1.0074	1.0090	1.0094
10	Thixotropic	0.0150	0.0150	0.0150	0.0149
	Newtonian	1.0 (-0.00345)	1.0070	1.0089	1.0092

Table 4: Pressure induced dimensionless torque normalized with respect to the Newtonian value for the corresponding rotational velocity. Absolute dimensionless value is given between braces.

ω	T'_p	M1	M2	M3	M4
1	Thixotropic	0.0654	0.0642	0.0634	0.0634
	Newtonian	1.0 (-0.00495)	0.9971	0.9956	0.9955
10	Thixotropic	0.0173	0.0172	0.0170	0.0170
	Newtonian	1.0 (-0.00495)	0.99713	0.9959	0.9957

5.2.2. Numerical convergence over S1 and S2 trajectories

Further exploration of mesh-convergence is performed by comparing Newtonian and thixo-viscoelastic solutions over the S1 (rotor wall) and S2 (arc between blades) trajectories in Fig. 7 and 8. In the case of S1 (Fig. 7), where a no-slip boundary condition is enforced and, thus, solutions are basically the same for all cases, we report solutions for pressure, which are relevant for estimating the forces acting on the blades and crucial for calculating their wear. In the S2 curve analysis (Fig. 8), however, inertial frame velocity is shown as a direct representation of the viscoelastic thinning response of Al-alloys. Overall, for pressure, velocity, strain-rate, fluidity, and stress plots over these trajectories are reported across meshes from M1 to M4.

As illustrated in Fig.7, Newtonian solutions (black lines-symbols) converge for both rotational speeds and appear markedly different when compared to the thixo-viscoelastic response (colored data). For the thixo-viscoelastic case, Fig. 8 shows a convergent response without perturbations, with overlapping features for all meshes. Their relative maximum differences, from M1 to M4 meshes, are: 0.001 for velocity, 0.05 for fluidity, 0.01 for stress,

and 0.02 for strain-rate. Solutions on the S1-wall trajectory in Fig. 7 display oscillations at points II, IV and VI, which correspond to locations near the rotor tips, for the thixo-viscoelastic case at both Wi-levels examined, being those at Wi=10 more exaggerated. This may be related to fluctuations happening in the internal structure of the material due to the relatively high strain-rate levels expected at those locations and the discrete solution representation. Nevertheless, away from those points, thixo-viscoelastic solutions converge consistently for both rotational speeds.

The oscillations on the S1 trajectory in Fig. 7 along the blade curve connecting points II, IV and VI for both Wi-levels may be explained as follows:

1. On one hand, oscillations at points II and VI are caused by local extrema near the blade tips that are responsive to mesh resolution. The regions where such extrema appear have been marked with white ellipses in Fig. 9. The sensitivity to mesh resolution stems from the high-fluidity layer located at blade tips as a consequence of shear-thinning and the relatively high strain-rates in those locations. Fluidity decays notably fast with distance from the blade, and hence non-Newtonian stress maxima are found next to blade surfaces, which can only be captured with high mesh resolution. The higher the Wi-value, the thinner the high-fluidity layer and the finer the mesh required to capture the solution accurately in those regions.

2. On the other hand, oscillations surrounding point IV stem from perturbations on velocity magnitude caused by a lower mesh quality of the inner rotor hub. Such velocity perturbations and the relatively higher fluidity in this region generate stresses that strongly couple with velocity. Nevertheless, when increasing mesh resolution, numerical errors reduce and strain-rate recovers a smooth distribution, except for two strong spikes at arclengths 0.48 and 0.64, located at the change from the planar blade to the curved hub. Indeed, even the Newtonian case shows small strain-rate oscillations at these locations with mesh refinement, as apparent in Fig.7 (b), which appear amplified in the viscoelastic case.

6. Numerical results of the stator-rotor mixer

In this section, Newtonian and viscoelastic solutions in a stator-rotor configuration are presented. Simulations were carried out using a single rotating frame-of-reference, as in the stator-free case, where the stator boundary conditions are $\boldsymbol{u} = 0$ for the inertial velocity.

The velocity field is represented in Fig.10. Both Newtonian solutions at $\omega = \{1, 10\}$ are equal in dimensionless form, as illustrated in Fig.10a. In contrast to the centered Newtonian vortex, the viscoelastic case at Wi=1 shows an expanded convex vortex, as in the stator-free case, a feature which appears shifted towards the stator. Conversely, the high Wi=10 case does not show the convex form of the stator-free case, but a concave shape as well; although not as pronounced as for Wi=1. The Newtonian solution is comparable with the high Wi case with imperceptible differences. The presence of the stator generates a restriction in the fluid circulation between the outside and the inside of the stator ring. The streamlines generated are circular-shaped, in contrast with the elliptical shape of the stator-free case. This mechanism generates the inter-blade vortex size amplification.

Regarding the material interchange between the mixing head and the outer bulk zone beyond the stator, inflow to the mixing head occurs through the stator gaps in front of the blade suction side, whereas the fluid is pushed outwards through the gap in front of the blade pressure side (arrows within Fig.10 represent such flow direction). Comparing the inflow and outflow speeds for the different cases, slightly higher peak and mean velocities are achieved for the Newtonian and high Wi viscoelastic cases compared with low Wi-flow. Hence, a less effective dispersion of sheared microstructure into the bulk fluid is achieved in the viscoelastic case at low frequencies.

Strain-rate results are presented in Figure 11. Larger maximum strain-rate values are achieved in all rotor-stator cases compared with the stator-free case, caused by the squeezing of the flow between the vortex or rotor and the stator.

Nevertheless, at Wi=1, low strain-rate values are still observed in the inter-blade vortex region, which develops strong viscoelastic behaviour as shown in Figure 12. In this region, Fig.12 (a) appears occupied by fully-structured material with fluidity approaching ϕ_0. Correspondingly, relatively large non-Newtonian stress forces are developed in this region, as illustrated in Fig.12 (c). In the rotor-stator gap zone, high non-Newtonian stress forces can also be observed despite the high fluidity in the area; this feature is related to the high strain-rates registered in such regions. It is noteworthy that the alternating viscoelastic stress patterns in between stator gaps affects the inflow/outflow velocity behavior, as already described.

The Wi=10 case, on the contrary, generates much milder non-Newtonian forces in all the domain, with vanishing non-Newtonian stress in the inner-most vortex region of the inter-blade zone, as shown in Fig.12 (d). High

fluidity values are generated in all the inner-stator domain. Therefore, the rotor-stator combination behaves closer to the Newtonian case compared to the stator-free case, in which the high strain-rate conditions provoke an extreme shear-thinning of the alloy.

Finally, the solution in the rotor-stator gap region is explored in Fig. 13. Fig. 13a shows the strain-rate value, which is the main variable of interest to monitor in the metal microstructure shearing context. The Newtonian and the Wi=10 cases show similar behaviour, whereas Wi=1 is around 75 % higher in the curve region between two consecutive blades. The difference rises up to 85 % higher strain-rate near the suction edge of the blade tip.

The viscoelastic fields are represented in Fig. 13 (b) and (c) and display an order-of-magnitude difference between both Wi solutions for stress and fluidity.

Both the pressure and viscous torque values are given in Table 5. Comparing the Newtonian results for the rotor-stator and stator-free cases, the first shows 5 times larger torque values than the open-rotor case. Such a difference is caused by the flow constriction generated by the stator. When comparing the thixotropic to Newtonian torque ratio for each case, the rotor-stator results show a thinning of 2 to 3 times larger than the open-rotor case. Hence, thixotropy becomes relevant in rotor-stator optimization.

Table 5: Viscosity and pressure induced dimensionless torque normalized with respect to the Newtonian value for the corresponding rotational velocity. Absolute dimensionless value is given between braces.

ω		T'_η	T'_p
1	Thixotropic	0.0126	0.0212
	Newtonian	1.0 (-0.017)	1.0 (-0.0239)
10	Thixotropic	0.0104	0.0113
	Newtonian	1.0 (-0.017)	1.0 (-0.0239)

6.1. Viscoelastic relevance in mixing-head design

The mixing head optimization is essential for shear-rate maximization in order to fragment deterrent intermetallic phases and achieve effective grain-refinement. The required strain-rate level to achieve an appropriate microstructure of the alloy is problem-dependent according to the alloy under consideration, the required solid state microstructure quality level, and the possible solidification speed though heat-transfer.

However, the main benefits of a rotor-stator mixing head are the following [56]: (i) high shear-rate values in the mixing head with oxide inclusions dispersion; (ii) a distributive mixing action that homogenizes temperature, chemical composition, and nucleation sites; and (iii) a laminar interaction between macroscopic bulk flow and the solidification front in continuous casting operations.

Viscoelasticity has revealed itself to confine the strain effects in a smaller area around the rotor-stator gap, giving rise to a higher strain-rate values compared to the pure Newtonian case. However, the fluid ejection through the stator holes is slowed down. Therefore, current viscoelastic laminar shear-rate mixing is understood to have better capacities than the Newtonian case to generate high shear-rate values but, probably, less effective distributive and homogenizing properties depending on the shear-rate in a particular operation. Since the current application is run under laminar conditions within the mixing head, the requirement of laminarization for the interaction with the sump of the caster can be relaxed to improve overall microstructure homogeneity when studying 3D effects, which might give rise to new rotor-stator combinations.

7. Conclusions

This research reports on the flow analysis of thixo-viscoelastic aluminium alloys at low/moderate temperatures near melting point, in open rotor and rotor-stator mixers using the Bautista-Manero-Puig (BMP) model, and the open-source rheoTool in OpenFOAM. The BMP-model parameters were tuned to reflect the alloys' extreme shear-thinning and time-dependent viscosity responses.

2D rotor and rotor-stator geometries were studied, and relevant field variables were reported, including viscoelastic stress and fluidity. When the stator is not included, a contrasting behaviour is found between the relatively inert Newtonian solutions and the strongly-varying thixo-viscoelastic case. This is linked to the change of fluidity of the BMP fluid in such regions, responding with highly-structured material at relatively smaller rotational speeds that thin and lose strength with rotation-rate rise. When a stator is included, the flow behaviour inside the stator region resembles the Newtonian case due to the fluidized material occupying most of the flow domain. However, the flow entering and exiting the stator region, and the overall flow circulation, are affected by the lower fluidity outside the stator area.

These contrasting trends could influence real-world aluminium alloy processing, particularly as thixo-viscoelastic properties emerge at processing temperatures near their melting point. In particular, contrasting features arise in the low-strain regions, as discussed in this paper, providing new insights on flow structure and thixo-viscoelastic alloy shearing and mixing.

8. Acknowledgements

This work has been partially funded by the Basque Government through the projects Elkartek CIRCU-AL : KK-2020/00016 and SosIAMet KK-2022/00110. Financial support through the BERC 2022-2025 program and by the Spanish State Research Agency through BCAM Severo Ochoa Excellence Accreditation CEX2021-001142-S/MICIN/AEI/10.13039/501100011033 is also acknowledged. Funding was also provided by the Provincial Council of Bizkaia within the Technology Transfer Programme 2021 with FEDER co-funding. JELA acknowledges the support from Consejo Nacional de Ciencias, Humanidades y Tecnologías (CONAHCYT, Mexico - grant number CF-2023-I-318) and from Universidad Nacional Autónoma de México UNAM (grant numbers PAPIIT IA102022 and PAIP 5000-9172 Facultad de Química).

References

[1] A. Flores-V, M. Sukiennik, A. Castillejos-E, F. Acosta-G, J. Escobedo-B, A kinetic study on the nucleation and growth of the al8femnsi2 intermetallic compound for aluminum scrap purification, Intermetallics 6 (3) (1998) 217–227.

[2] J. Yang, F. Yin, improvement of the morphology of iron phase in al-si alloys, Foundry 49 (80) (2000) 454–459.

[3] F. Yin, J. Yang, Y. Wang, G. Wang, effect of mn and be on the iron-phase in al-si alloys, Foundry 49 (2000) 829–831.

[4] S. Shabestari, M. Mahmudi, M. Emamy, J. Campbell, Effect of mn and sr on intermetallics in fe-rich eutectic al-si alloy, International Journal of Cast Metals Research 15 (1) (2002) 17–24.

[5] M. Mahta, M. Emamy, A. Daman, A. Keyvani, J. Campbell, Precipitation of fe rich intermetallics in cr-and co-modified a413 alloy, International Journal of Cast Metals Research 18 (2) (2005) 73–79.

[6] M. Mahta, M. Emamy, X. Cao, J. Campbell, V. Lawrence, N. Olivante, Overview of β-al5fesi phase in al-si alloys, Materials Science Research Trends (2008) 251–271.

[7] F. Simbarashe, J. Li, Q. D. Hu, Purification of an industrial aluminum alloy by melt stirring during ohno continuous casting process, Journal of Chemical Engineering and Materials Science 2 (3) (2011) 44–52.

[8] C. Kang, J. Bae, B. Kim, The grain size control of a356 aluminum alloy by horizontal electromagnetic stirring for rheology forging, Journal of Materials Processing Technology 187 (2007) 344–348.

[9] K. Jackson, J. Hunt, Trans. met. soc, in: AIME, Vol. 236, 1966, p. 1129.

[10] M. C. Flemings, Behavior of metal alloys in the semisolid state, Metallurgical transactions A 22 (5) (1991) 957–981.

[11] D. L. McRae, R. D. Willans, E. L. Mawer, Method for agitating metals and producing alloys, uS Patent 4,743,428 (May 10 1988).

[12] Z. Fan, B. Jiang, Y. Zuo, Apparatus and method for liquid metals treatment, uS Patent App. 13/823,216 (Sep. 5 2013).

[13] E. L. Paul, V. A. Atiemo-Obeng, S. M. Kresta, Handbook of industrial mixing, Wiley Online Library, 2004.

[14] M. Tong, J. B. Patel, I. Stone, Z. Fan, D. J. Browne, Identification of key liquid metal flow features in the physical conditioning of molten aluminium alloy with high shear processing, Computational Materials Science 131 (2017) 35–43.

[15] K. Solek, S. Szczepanik, Rheological analysis of semi-solid a380.0 aluminium alloy, Arch. Metall. Mater. 60 (2015) 2613–2617.

[16] X. Yang, Y. Jing, J. Liu, The rheological behavior for thixocasting of semi-solid aluminum alloy (a356), Journal of materials processing technology 130 (2002) 569–573.

[17] B. Meylan, S. Terzi, C. Gourlay, A. Dahle, Dilatancy and rheology at 0–60% solid during equiaxed solidification, Acta Materialia 59 (8) (2011) 3091–3101.

[18] R. Wang, W. Cao, J.-M. Zhang, Dependency of dilatancy ratio on fabric anisotropy in granular materials, Journal of Engineering Mechanics 145 (10) (2019) 04019076.

[19] B. Ouriev, Rheology and rheometry of aluminum alloys: Influence of shear and vibration on aluminum flow properties, in: Solid State Phenomena, Vol. 116, Trans Tech Publ, 2006, pp. 558–564.

[20] P. Das, S. K. Samanta, H. Chattopadhyay, P. Dutta, N. Barman, Rheological characterization of semi-solid a356 aluminium alloy, in: Solid State Phenomena, Vol. 192, Trans Tech Publ, 2013, pp. 329–334.

[21] M. Modigell, A. Pola, M. Tocci, Rheological characterization of semi-solid metals: a review, Metals 8 (4) (2018) 245.

[22] L. Orgeas, J. Gabathuler, T. Imwinkelried, C. Paradies, M. Rappaz, Modelling of semi-solid processing using a modified temperature-dependent power-law model, Modelling and simulation in Materials Science and Engineering 11 (4) (2003) 553.

[23] J. Fu, K. Wang, Modelling and simulation of die casting process for a356 semi-solid alloy, Procedia Engineering 81 (2014) 1565–1570.

[24] H. V. Atkinson, D. Liu, Microstructural coarsening of semi-solid aluminium alloys, Materials Science and Engineering: A 496 (1-2) (2008) 439–446.

[25] P. Das, M. Kumar, S. K. Samanta, P. Dutta, D. Ghosh, Semisolid processing of a380 al alloy using cooling slope, Materials and Manufacturing Processes 29 (4) (2014) 422–428.

[26] P. Das, S. K. Samanta, S. Bera, P. Dutta, Microstructure evolution and rheological behavior of cooling slope processed al-si-cu-fe alloy slurry, Metallurgical and Materials Transactions A 47 (5) (2016) 2243–2256.

[27] C. Sellars, Q. Zhu, Microstructural modelling of aluminium alloys during thermomechanical processing, Materials Science and Engineering: A 280 (1) (2000) 1–7.

[28] W. Dijkstra, C. Vuik, L. Katgerman, Network model of fluid flow in semi-solid aluminum alloys, Computational materials science 38 (1) (2006) 67–74.

[29] B. Wu, M. Li, D. Ma, The flow behavior and constitutive equations in isothermal compression of 7050 aluminum alloy, Materials Science and Engineering: A 542 (2012) 79–87.

[30] X. Hu, Q. Zhu, H. Atkinson, H. Lu, F. Zhang, H. Dong, Y. Kang, A time-dependent power law viscosity model and its application in modelling semi-solid die casting of 319s alloy, Acta Materialia 124 (2017) 410–420.

[31] P. Coussot, Q. D. Nguyen, H. Huynh, D. Bonn, Avalanche behavior in yield stress fluids, Physical review letters 88 (17) (2002) 175501.

[32] A. N. Alexandrou, G. Georgiou, On the early breakdown of semisolid suspensions, Journal of non-newtonian fluid mechanics 142 (1-3) (2007) 199–206.

[33] F. Hosseini Yekta, S. Sadough Vanini, Simulation the flow of semi-solid steel alloy using an enhanced model, Metals and Materials International 21 (5) (2015) 913–922.

[34] G. Chao, C. Wei, L. Yan-ming, Application of deform-3d software in optimizing forging stock shape of blade, Hot Working Technology 36 (1) (2007) 74–76, https://en.cnki.com.cn/Article_en/CJFDTOTAL-SJGY200701024.htm.
URL https://lens.org/067-183-496-839-577

[35] A. F. Bastani, T. Aukrust, S. Brandal, Optimisation of flow balance and isothermal extrusion of aluminium using finite-element simulations, Journal of Materials Processing Technology 211 (4) (2011) 650–667.

[36] I. Alfaro, D. Bel, E. Cueto, M. Doblaré, F. Chinesta, Three-dimensional simulation of aluminium extrusion by the α-shape based natural element method, Computer Methods in Applied Mechanics and Engineering 195 (33-36) (2006) 4269–4286.

[37] P. Cleary, J. Ha, V. Alguine, T. Nguyen, Flow modelling in casting processes, Applied Mathematical Modelling 26 (2) (2002) 171–190.

[38] P. Cleary, J. Ha, M. Prakash, T. Nguyen, 3d sph flow predictions and validation for high pressure die casting of automotive components, Applied Mathematical Modelling 30 (11) (2006) 1406–1427.

[39] P. Cleary, M. Prakash, J. Ha, Novel applications of smoothed particle hydrodynamics (sph) in metal forming, Journal of materials processing technology 177 (1-3) (2006) 41–48.

[40] M. Ellero, M. Kröger, S. Hess, Viscoelastic flows studied by smoothed particle dynamics, Journal of Non-Newtonian Fluid Mechanics 105 (1) (2002) 35–51.

[41] M. Ellero, R. Tanner, Sph simulations of transient viscoelastic flows at low reynolds number, Journal of Non-Newtonian Fluid Mechanics 132 (1-3) (2005) 61–72.

[42] M. Prakash, P. W. Cleary, Modelling highly deformable metal extrusion using sph, Computational Particle Mechanics 2 (1) (2015) 19–38.

[43] V. Favier, H. Atkinson, Micromechanical modelling of the elastic–viscoplastic response of metallic alloys under rapid compression in the semi-solid state, Acta Materialia 59 (3) (2011) 1271–1280.

[44] F. Bautista, J. de Santos, J. Puig, O. Manero, Understanding thixotropic and antithixotropic behavior of viscoelastic micellar solutions and liquid crystalline dispersions. i. the model, J. Non-Newton. Fluid Mech. 80 (1999) 93–113.

[45] J. E. López-Aguilar, M. F. Webster, H. R. Tamaddon-Jahromi, O. Manero, Predictions for circular contraction-expansion flows with viscoelastoplastic & thixotropic fluids, J. Non-Newton. Fluid Mech. 261 (2018) 188–210.

[46] J. E. López-Aguilar, O. Resendiz-Tolentino, H. R. Tamaddon-Jahromi, M. Ellero, O. Manero, Flow past a sphere: Numerical predictions of thixo-viscoelastoplastic wormlike micellar solutions, J. Non-Newton. Fluid Mech. 309 (2022) 104902.

[47] H. G. Weller, G. Tabor, H. Jasak, C. Fureby, A tensorial approach to computational continuum mechanics using object-oriented techniques, Computers in physics 12 (6) (1998) 620–631.

[48] F. Pimenta, M. Alves, Stabilization of an open-source finite-volume solver for viscoelastic fluid flows, Journal of Non-Newtonian Fluid Mechanics 239 (2017) 85–104. doi:https://doi.org/10.1016/j.jnnfm.2016.12.002.
URL https://www.sciencedirect.com/science/article/pii/S0377025716303329

[49] Y. Wu, S. Li, S. Liu, H.-S. Dou, Z. Qian, Vibration of hydraulic machinery, Springer, 2013.

[50] F. Pimenta, M. Alves, rheotool, https://github.com/fppimenta/rheoTool (2016).

[51] C. Fernandes, M. Araujo, L. Ferrás, J. Miguel Nóbrega, Improved both sides diffusion (ibsd): A new and straightforward stabilization approach for viscoelastic fluid flows, J. Non-Newton. Fluid Mech. 249 (2017) 63–78.

[52] F. Bautista, J. H. Pérez-López, J. P. García, J. E. Puig, O. Manero, Stability analysis of shear banding flow with the bmp model, J. Non-Newton. Fluid Mech. 144 (2007) 160169.

[53] J. E. López-Aguilar, H. R. Tamaddon-Jahromi, O. Manero, Shear banding predictions for wormlike micellar systems under a contraction-expansion complex flow, Phys. Fluids 35 (2023) 063101.

[54] F. Habla, A. Woitalka, S. Neuner, O. Hinrichsen, Development of a methodology for numerical simulation of non-isothermal viscoelastic fluid flows with application to axisymmetric 4: 1 contraction flows, Chemical engineering journal 207 (2012) 772–784.

[55] J. E. López-Aguilar, M. F. Webster, H. R. Tamaddon-Jahromi, O. Manero, Convoluted models and high-weissenberg predictions for micellar thixotropic fluids in contractionexpansion flows, J. Non-Newton. Fluid Mech. 232 (2016) 55–66.

[56] S. Jones, A. Prasada Rao, Z. Fan, Melt conditioned direct chill (mc-dc) casting of al alloys, Transactions of the Indian Institute of Metals 66 (2) (2013) 117–121.

List of Figures

1 Top: Steady shear-viscosity against shear-rate; Bottom: Transient shear-viscosity against time as a function a step shear-rate history (continuous grey lines). Steady state viscosity values correspond to the plateaux recorded at each shear-rate imposed in the transient test. Symbols: experiments in [15]; continuous lines: BMP model fitting. 31
2 Schematics of the open rotor geometry and M1, M2, M3 and M4 meshes. Discretization details are given in Table 2. 32
3 Geometry and mesh details for rotor-stator device. 33
4 Dimensionless field variables obtained according to Eq. 9 at 1 and 10 rad/s. Figures (a) and (h) correspond to identical Newtonian results for both rotational speeds. Viscoelastic solutions (b)-(g) and (i)-(j) correspond to the viscoelastic cases. 34
5 Strain-rate at 1 rad/s (a) and (c), and 10 rad/s (b) and (d) . . 35
6 field variables for Newtonian (a) and (b), and viscoelastic fluids (c) and (d) 36
7 Dimensionless field variables along curve S1. Mesh convergence is provided with discontinuous light discontinouus lines (colors online) 37
8 Dimensionless field variables along curve S2. Mesh convergence is provided with discontinuous light discontinouus lines (colors online) 38
9 Dimensionless τ_{eq}, fluidity and strain-rate at blade tips for 1 and 10 rad/s 39
10 Dimensionless Newtonian and Viscoelastic velocity at 1 and 10 rad/s. 40
11 Dimensionless Newtonian and Viscoelastic strain-rate at 1 and 10 rad/s. 9 at 1 and 10 rad/s. 41
12 Dimensionless Newtonian and Viscoelastic strain-rate at 1 and 10 rad/s. 9 at 1 and 10 rad/s. 42
13 Dimensionless field variables along curve S2 for the rotor-stator mixer head. 43

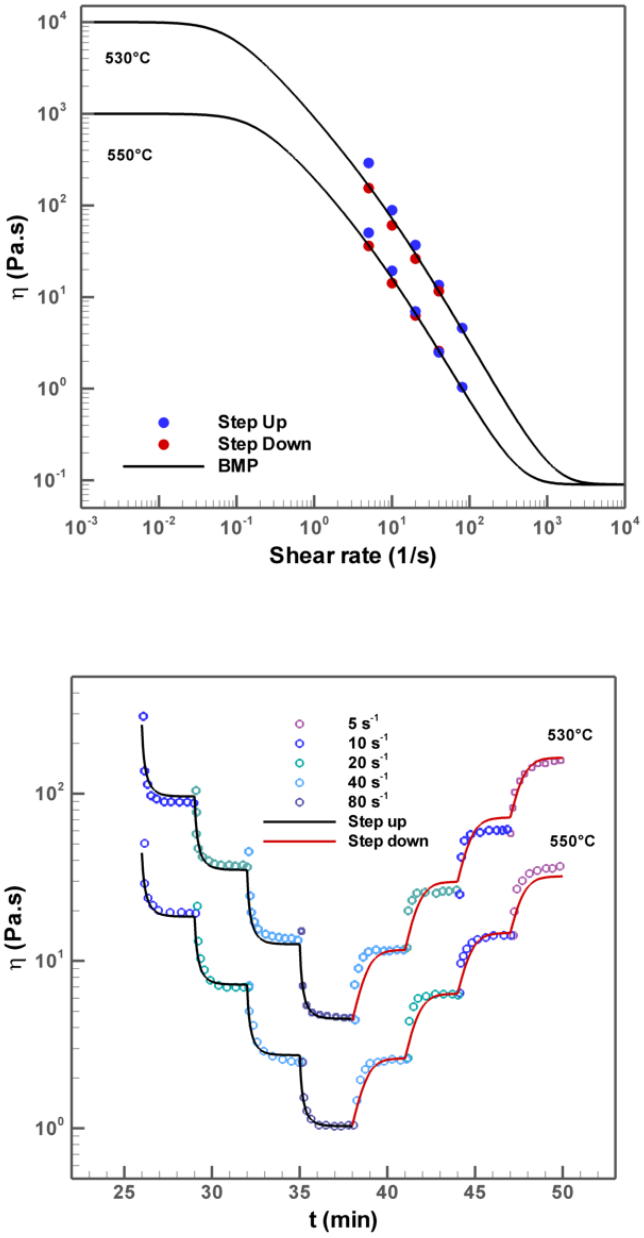

Figure 1: Top: Steady shear-viscosity against shear-rate; Bottom: Transient shear-viscosity against time as a function a step shear-rate history (continuous grey lines). Steady state viscosity values correspond to the plateaux recorded at each shear-rate imposed in the transient test. Symbols: experiments in [15]; continuous lines: BMP model fitting.

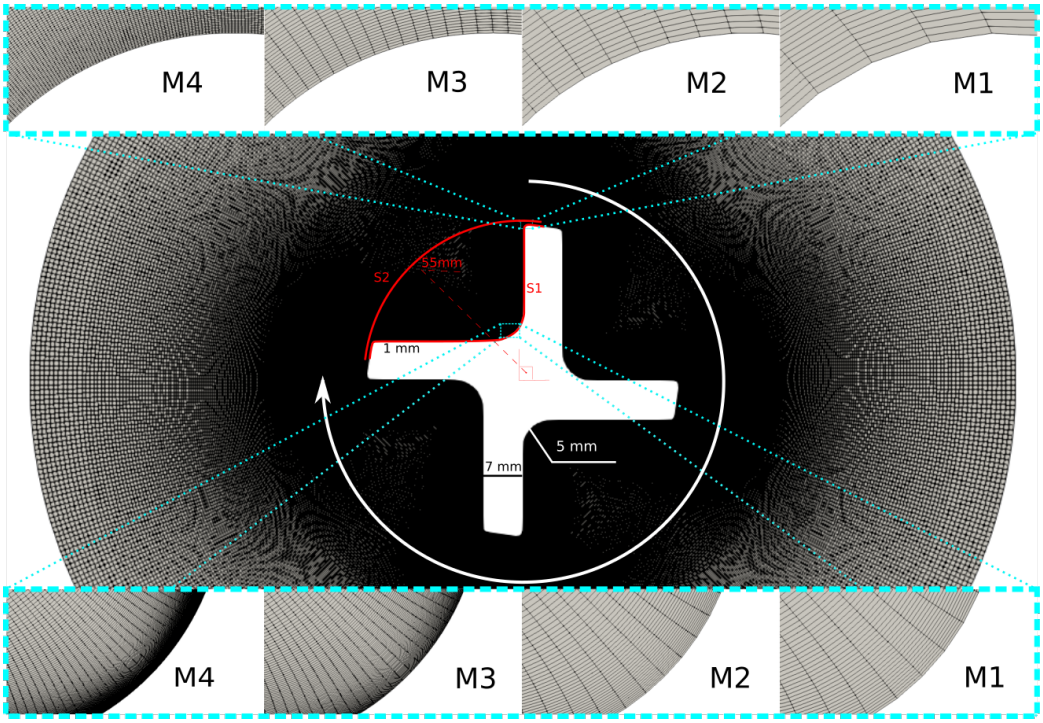

Figure 2: Schematics of the open rotor geometry and M1, M2, M3 and M4 meshes. Discretization details are given in Table 2.

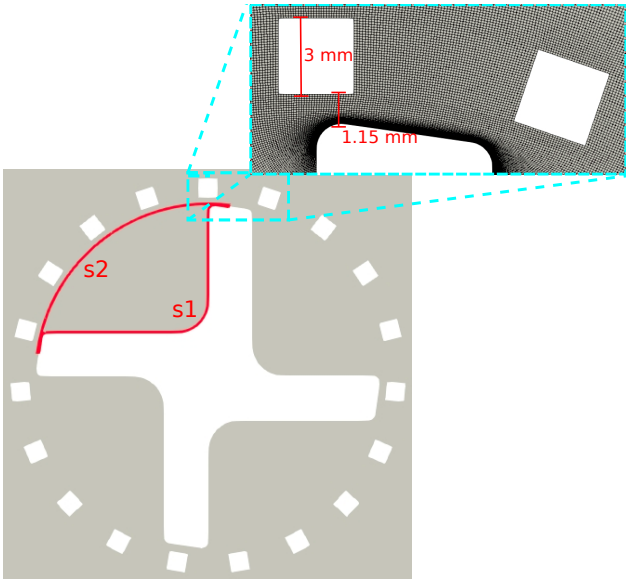

Figure 3: Geometry and mesh details for rotor-stator device.

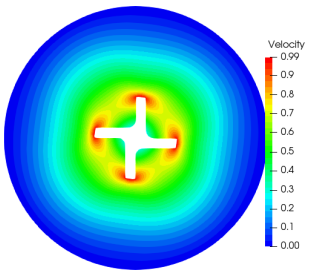

(a) Newtonian velocity solution, identical for 1 and 10 rad/s

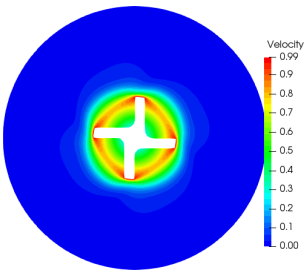

(b) velocity at 1 rad/s

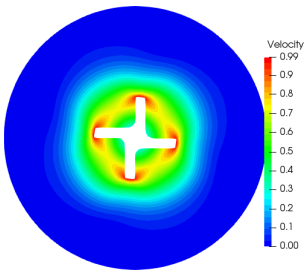

(c) velocity at 10 rad/s

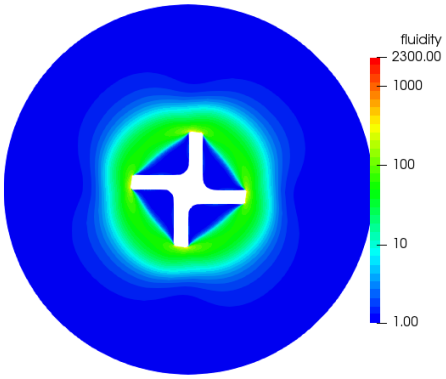

(d) fluidity at 1 rad/s

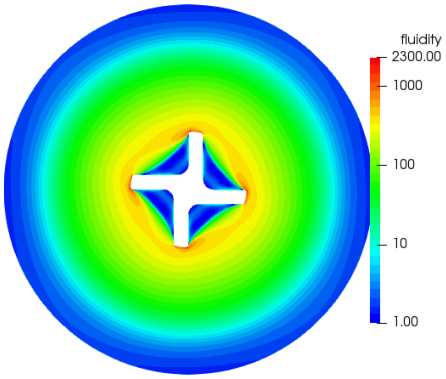

(e) fluidity at 10 rad/s

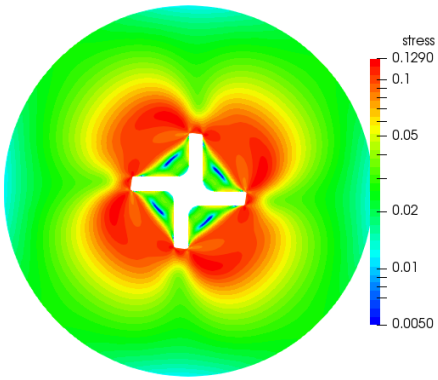

(f) τ_{eq} at 1 rad/s

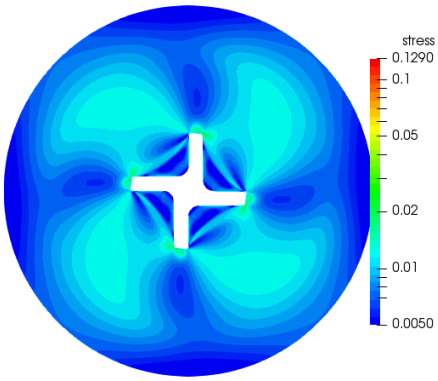

(g) τ_{eq} at 10 rad/s

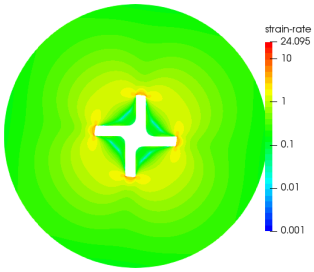

(h) Newtonian strain-rate, identical for 1 and 10 rad/s

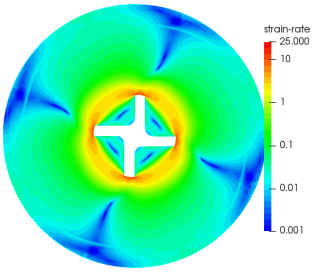

(i) strain-rate at 1 rad/s

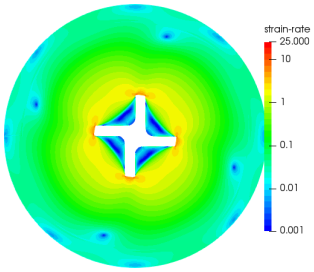

(j) strain-rate at 10 rad/s

Figure 4: Dimensionless field variables obtained according to Eq. 9 at 1 and 10 rad/s. Figures (a) and (h) correspond to identical Newtonian results for both rotational speeds. Viscoelastic solutions (b)-(g) and (i)-(j) correspond to the viscoelastic cases.

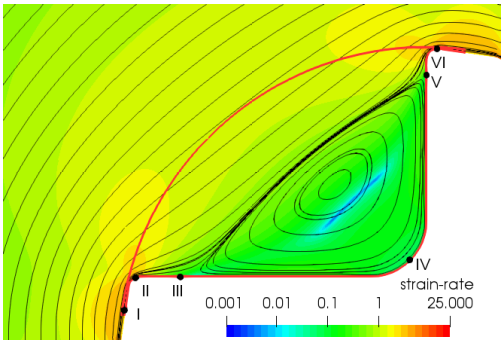

(a) Newtonian strain-rate at 1 rad/s

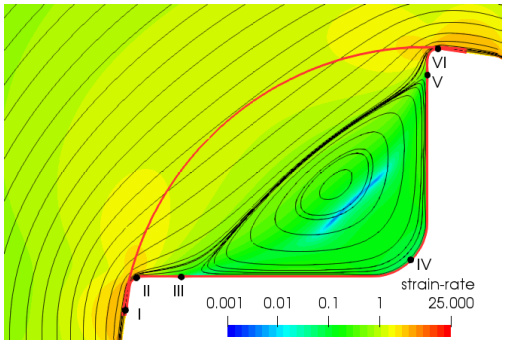

(b) Newtonian strain-rate at 10 rad/s

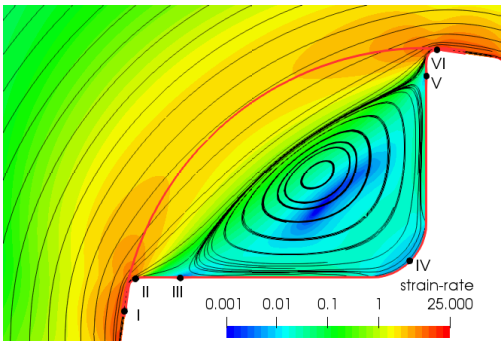

(c) viscoelastic strain-rate at 1 rad/s

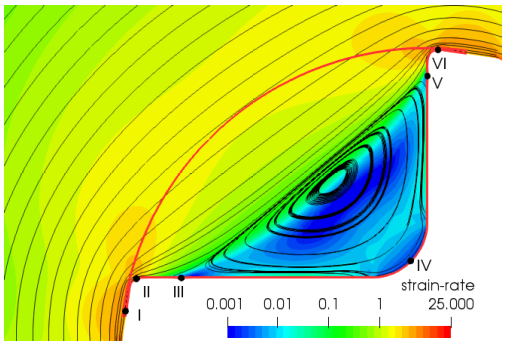

(d) viscoelastic strain-rate at 10 rad/s

Figure 5: Strain-rate at 1 rad/s (a) and (c), and 10 rad/s (b) and (d)

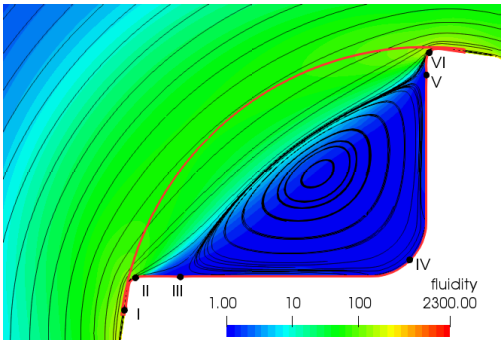

(a) viscoelastic fluidity at 1 rad/s

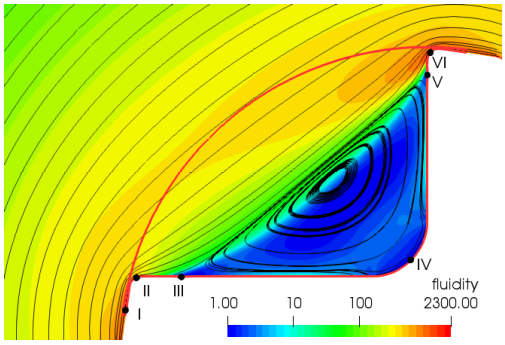

(b) viscoelastic fluidity at 10 rad/s

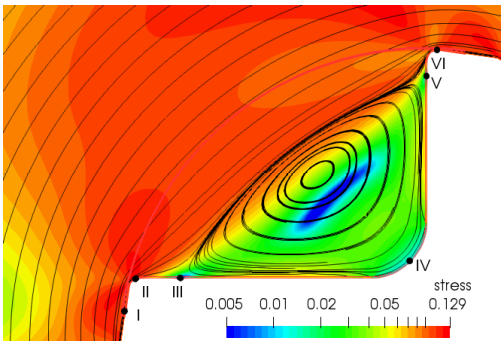

(c) viscoelastic τ_{eq} at 1 rad/s

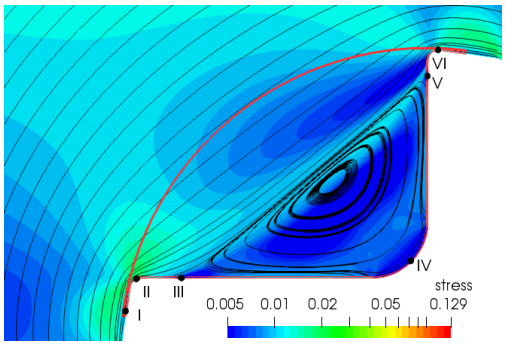

(d) viscoelastic τ_{eq} at 10 rad/s

Figure 6: field variables for Newtonian (a) and (b), and viscoelastic fluids (c) and (d)

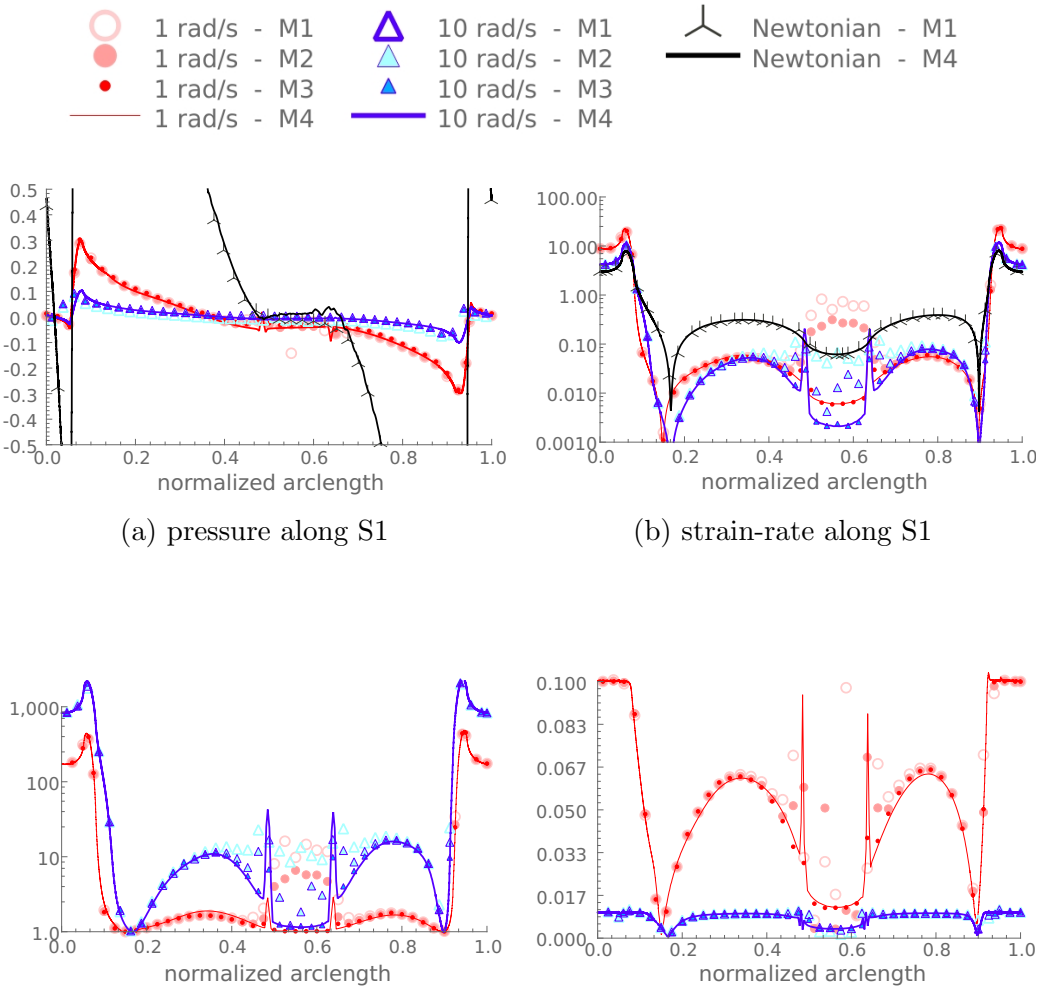

(a) pressure along S1

(b) strain-rate along S1

(c) fluidity along S1

(d) τ_{eq} along S1.

Figure 7: Dimensionless field variables along curve S1. Mesh convergence is provided with discontinuous light discontinouus lines (colors online)

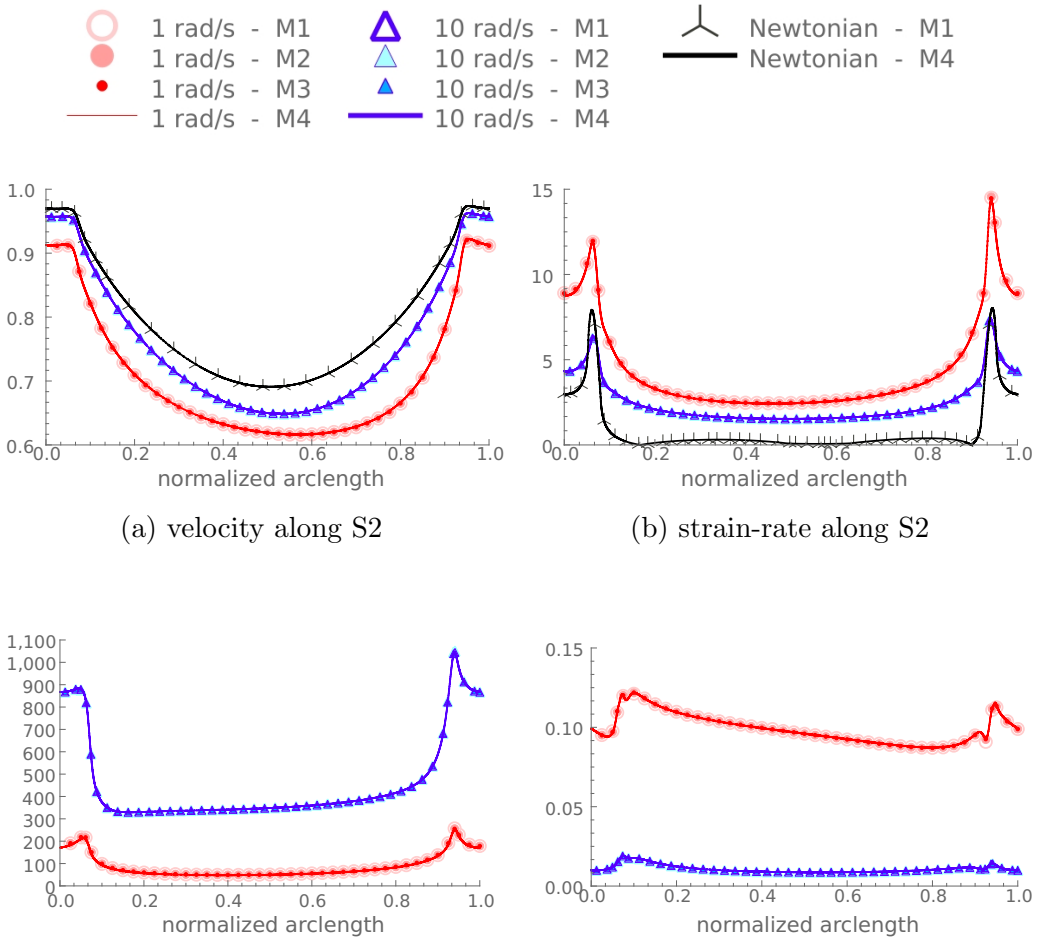

(a) velocity along S2

(b) strain-rate along S2

(c) fluidity along S2

(d) τ_{eq} along S2

Figure 8: Dimensionless field variables along curve S2. Mesh convergence is provided with discontinuous light discontinouus lines (colors online)

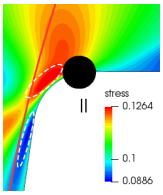

(a) point II τ_{eq} at 1 rad/s

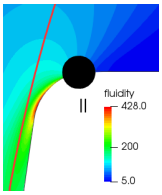

(b) point II fluidity at 1 rad/s

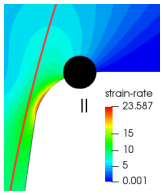

(c) point II strain-rate at 1 rad/s

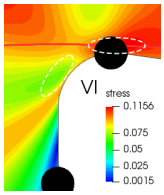

(d) point VI τ_{eq} at 1 rad/s

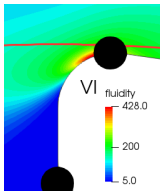

(e) point VI fluidity at 1 rad/s

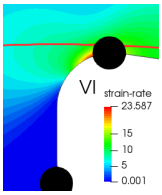

(f) point VI strain-rate at 1 rad/s

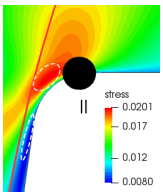

(g) point II τ_{eq} at 10 rad/s

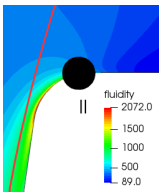

(h) point II fluidity at 10 rad/s

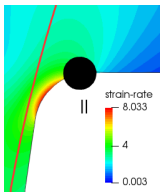

(i) point II strain-rate at 10 rad/s

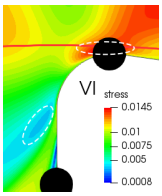

(j) point VI τ_{eq} at 10 rad/s

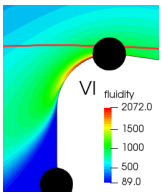

(k) point VI fluidity at 10 rad/s

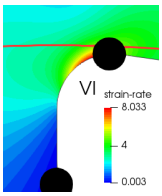

(l) point VI strain-rate at 10 rad/s

Figure 9: Dimensionless τ_{eq}, fluidity and strain-rate at blade tips for 1 and 10 rad/s

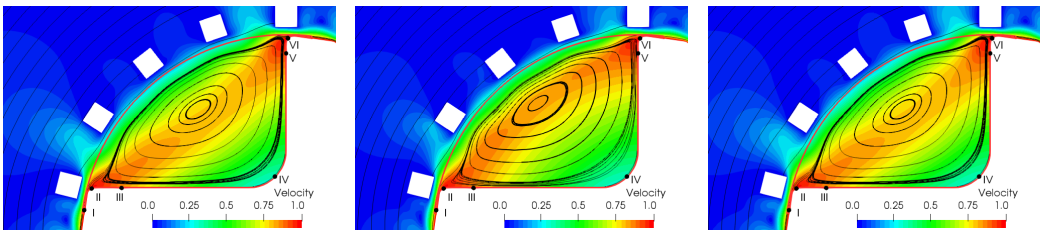

(a) Newtonian velocity solution at 10 rad/s with stator

(b) Viscoelastic velocity at 1 rad/s with stator

(c) Viscoelastic velocity at 10 rad/s with stator

Figure 10: Dimensionless Newtonian and Viscoelastic velocity at 1 and 10 rad/s.

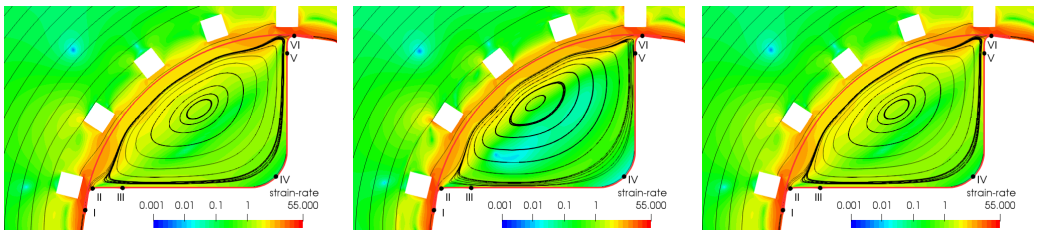

(a) Newtonian strain-rate solution at 10 rad/s with stator

(b) Viscoelastic strain-rate at 1 rad/s with stator

(c) Viscoelastic strain-rate at 10 rad/s with stator

Figure 11: Dimensionless Newtonian and Viscoelastic strain-rate at 1 and 10 rad/s. 9 at 1 and 10 rad/s.

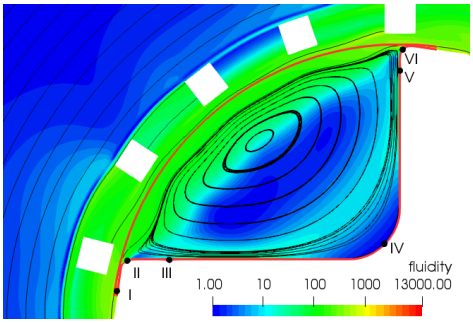

(a) Viscoelastic fluidity solution at 1 rad/s with stator

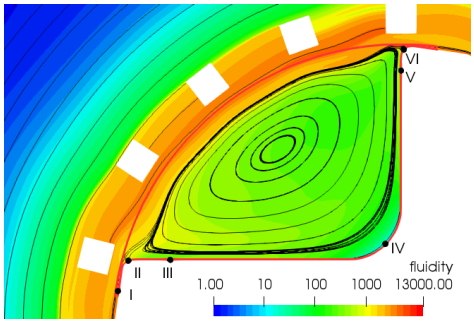

(b) Viscoelastic fluidity solution at 10 rad/s with stator

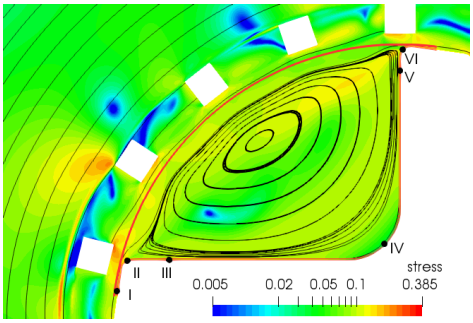

(c) Viscoelastic τ_{eq} at 1 rad/s with stator

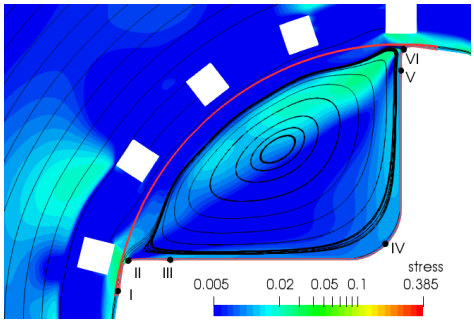

(d) Viscoelastic τ_{eq} at 10 rad/s with stator

Figure 12: Dimensionless Newtonian and Viscoelastic strain-rate at 1 and 10 rad/s. 9 at 1 and 10 rad/s.

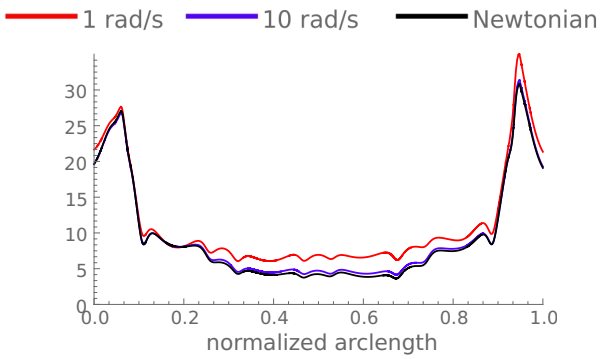

(a) strain-rate along S2

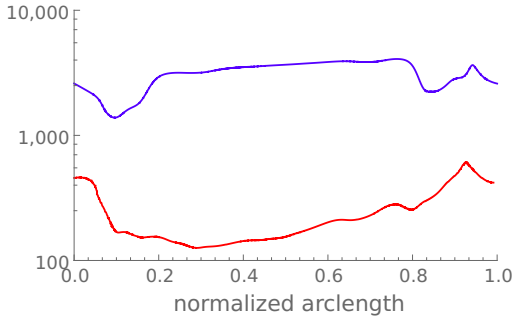

(b) fluidity along S2

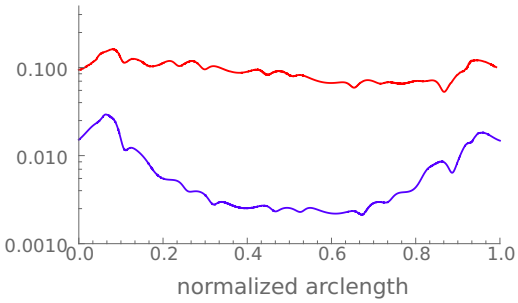

(c) Non-Newtonian τ_{eq} along S2

Figure 13: Dimensionless field variables along curve S2 for the rotor-stator mixer head.